N/Z equilibration in damped collisions induced by $E/A = 8.5$ MeV ^{58}Ni and ^{64}Ni on ^{238}U

R. Planeta,* S. H. Zhou,† K. Kwiatkowski, W. G. Wilson,‡ and V. E. Viola
Department of Chemistry and Indiana University Cyclotron Facility, Indiana University, Bloomington, Indiana 47405

H. Breuer, D. Benton,§ and F. Khazaie**
Department of Physics, University of Maryland, College Park, Maryland 20742

R. J. McDonald
Nuclear Sciences Division, Lawrence Berkeley Laboratory, Berkeley, California 94720

A. C. Mignerey and A. Weston-Dawkes
Department of Chemistry, University of Maryland, College Park, Maryland 20742

R. T. de Souza, J. R. Huizenga, and W. U. Schröder
Department of Chemistry and Nuclear Science Research Laboratory, University of Rochester, Rochester, New York 14627

(Received 16 March 1988)

Nuclide distributions have been measured for damped collision products formed in the reaction of $E/A = 8.5$ MeV ^{58}Ni and ^{64}Ni ions with ^{238}U. The data demonstrate that in these very asymmetric systems the evolution of the nucleon-exchange process as a function of energy loss depends strongly on the N/Z value of the projectile and the corresponding gradient in the potential-energy surface. Comparison of the data with transport model calculations shows qualitative agreement with the N and Z centroids, variances, and correlation coefficients. However, absolute discrepancies exist which suggest the need for improvement in the model.

I. INTRODUCTION

Valuable insight into the underlying mechanisms which govern the evolution of damped heavy-ion collisions can be derived from studies of product mass and charge distributions as a function of dissipated energy. Previous studies of this nature have provided convincing support for the stochastic exchange of nucleons, accompanied by the conversion of relative kinetic energy into internal excitation energy, as the primary mechanism for damped collisions.[1,2] In the transport models conceived to describe these processes,[3-6] the centroids of the product nuclide distributions define the mean drift in the number of nucleons transferred, reflecting the local gradient in the potential-energy (PES); the variances represent the average number of nucleons exchanged, and the neutron-proton correlation coefficients arise from effects associated with the curvature and alignment of the PES. A thorough review of these concepts can be found in Refs. 1 and 2.

While existing nucleon-exchange theories have met considerable success in accounting for numerous features of damped collisions, many important uncertainties remain. For example, the models frequently fail to reproduce the dependence of the neutron and proton drifts on energy loss for asymmetric target-projectile systems.[7,8] This situation may be due to inadequacies in the dynamics associated with the formation of the dinuclear complex and/or the potential energy surfaces used in the transport model calculations. Discrepancies between experiment and theory are most noticeable in accounting for the N/Z equilibration process for partially-damped events, for which Q-value or dynamical effects might be expected to influence nucleon-exchange most strongly. These differences may be indicative of contributions from other mechanisms; e.g., simple nuclear-transfer reactions, collective charge transfer via excitation of isovector giant resonances, or Gamow-Teller charge exchange.[9-11] The importance of such relatively fast processes remains an important open question in the study of damped collisions.[2]

In an earlier study[12] the dependence of projectile-like-fragment nuclidic yields on target mass was investigated in ^{56}Fe-induced reactions at $E/A = 8.3$ MeV. These measurements explored the dependence of the nucleon-exchange process on target-projectile mass asymmetry for systems ranging from ^{56}Fe + ^{56}Fe to ^{56}Fe + ^{238}U. In this work emphasis was placed on the acquisition of simultaneous, high-resolution Z and A distributions as a function of energy loss in order to provide high-quality data for the centroids, variances, correlation coefficients, and conditional variances for these reactions. In particular, analysis of the ^{56}Fe + ^{238}U system revealed important deviations from transport model calculations and also highlighted the critical role of excitation-energy division in the interpretation of damped collision results.[7,12] This latter problem has also been studied recently and it has been shown that excitation-energy sharing evolves from near equipartition in the quasielastic region (as reported previously) to a value near the mass ratio of the fragments for fully damped events.[13-17] The functional form of the excitation sharing exerts an important influence on both the calculation of energy loss and the comparison of theoretical and experimental results.

The objective of the present studies was to extend the previous investigations of the nucleon-exchange process to similar mass-asymmetric systems with distinctly different neutron-proton ratios and potential-energy surfaces. Earlier comparisons of discrete Z and A distributions obtained for the ^{40}Ca + ^{64}Ni and ^{40}Ar + ^{58}Ni systems[18] suggested that the N/Z ratio of the damped products adjusts to the N/Z of the composite systems at very low energy-loss values. This result has been interpreted to mean that N/Z equilibration occurs on a time scale significantly faster than energy equilibration. However, the exchange of one pair of nucleons is nearly sufficient to equilibrate these systems and subsequent studies of more asymmetric, heavier systems[8,12,19] have demonstrated that N/Z equlibration is a monotonic, continuous process that is not completed until nearly complete energy damping is achieved.

For the present studies we have chosen to bombard ^{238}U with ^{58}Ni and ^{64}Ni projectiles at $E/A=8.5$ MeV. The choice of ^{238}U as a target ($N/Z=1.59$) ensures maximum mass asymmetry in the entrance channel and in addition complements similar existing results for ^{56}Fe + ^{238}U (Ref. 12) and ^{40,48}Ca + ^{238}U (Ref. 20) at this bombarding energy. The projectiles ^{58}Ni ($N/Z=1.07$) and ^{64}Ni ($N/Z=1.29$) provide a wide range of neutron-proton asymmetry and at the same time insure that a major fraction of the reaction cross section, σ_R, goes into the damped collision channel, $\sigma_{\rm DC}$, ($\sigma_{\rm DC}/\sigma_R \cong 0.92$).[21] The bombarding energy of $E/A=8.5$ MeV provides a wide range of energy dissipation (up to $\sim$200 MeV), while at the same time minimizing the effects of precompound events or projectile splitting, which would contaminate the spectra at higher bombarding energies.

We first discuss the experimental technique and data analysis procedures. This is followed by a presentation of the experimental data, after which the results are compared with the predictions of a microscopic transport model calculation.[22] These data are also compared with results for the reaction of ^{40}Ca, ^{48}Ca, and ^{56}Fe ions with ^{238}U at a similar energy, which show a striking dependence of the nucleon drift on projectile N/Z ratio.

II. EXPERIMENTAL PROCEDURES

The detector system, experimental details, and data reduction procedures are described in this section. For a more thorough discussion of these techniques the reader is referred to Ref. 23 for details of the nuclide-identification detector system and to Refs. 12 and 24 for discussion of the data analysis and fitting procedures.

A. Experiment

The measurements were performed in the 30-in.-diameter scattering chamber at the Lawrence Berkeley Laboratory SuperHILAC with 494 MeV ^{58}Ni and 534 MeV ^{64}Ni beams. A self-supporting ^{238}U target of thickness 490 μg/cm^2 was bombarded with Ni beams ranging in intensity from 50 to 500 nA. The target ladder was electrically isolated from the scattering chamber and a voltage of + 15 kV was applied to suppress secondary electrons emitted from the target. In addition, Sm-Co magnets were placed after the first collimator in order to suppress electrons. The first collimator was an electropolished 8 mm diameter aperture, covered by a 110 μg/cm^2 nickel foil to suppress low-energy photons.

In order to derive fast-timing signals for precision time-of-flight determination, secondary electrons emitted from a 30 μg/cm^2 carbon foil placed in the fragment flight path were accelerated onto a pair of microchannel plates.[23] To minimize deadtime effects associated with exposure of the channel plates to the beam-target interaction region, the channel-plate devices were operated in a reverse configuration; i.e., electrons emitted in the backward direction were used to trigger the timing system. The first timing element (CP1) was placed with its carbon foil 24 cm from the target and utilized a pair of 18 mm active-diameter channel plates. The second element (CP2), which employed 40 mm diameter plates and a 40 μg/cm^2 polypropylene foil covered with 60 nm of aluminum, was positioned 120 cm downstream from CP1 in a vacuum box connected to the sliding-seal port of the scattering chamber. Using commercially available fast-timing electronics, this system yielded a timing resolution of better than 120 psec [full width at half-maximum (FWHM)] for elastically scattered Ni ions. For this time resolution and flight path, the major contribution to the mass resolution was the energy resolution of the ΔE-ΔE-E detector telescope. A series of antiscattering baffles and electropolished stainless steel apertures was placed along the time-of-flight path to reduce anomalous scattering effects.

Fragment energy and charge identification were obtained with an x-y position-sensitive ΔE-ΔE-E detector telescope[23] which followed the CP2 timing device. Energy-loss (ΔE-ΔE) measurements were performed via a segmented gridded gas-ionization chamber housed in a common detector box. Fragments were stopped in a 100 μm silicon surface barrier (E) detector of area 900 mm^2, operated within the gas-ionization chamber. The gas-ionization chamber (GIC) used CF$_4$ at 32 Torr as a working gas. Isolation between the GIC gas volume and the scattering chamber and extension port vacuum ($\sim 3\times 10^{-6}$ Torr) was maintained with a stretched polypropylene foil. The two ΔE segments were separated by an aluminum shield with an aperture of 3.6 cm diameter along the fragment flight path. The anode plates and Frisch grids in the two segments were placed parallel to the fragment path, but were oriented at 90° with respect to one another. By operating a time-to-amplitude converter between the anode signal of each ΔE detector and the silicon E detector signal, it was possible to use the electron drift time to achieve a position resolution of 0.3 mm in both x and y dimensions. The resultant position sensitivity was a critical factor in obtaining the final Z and A resolution reported in this work, since it enabled precise calculations of corrections arising from geometric differences in fragment flight paths and variable gas thicknesses in the first ΔE element caused by bowing of the GIC window foil.

The silicon surface barrier E detector was located 175 cm from the target and collimated with a 33-mm-diameter aperture. This defined a solid angle of 0.28 msr. A fast timing pickoff on this detector was used to provide redundant timing information with both channel-plate signals. For both the ^{58}Ni and ^{64}Ni beams, measurements were performed at 41°, near the peak of the angular distribution for damped collision products. This permitted a sampling of the full range of damping with good statistics and also minimized contributions from any orbiting component in the data. A total of 2.1×10^6 events was accumulated for ^{58}Ni and 4.9×10^5 events for ^{64}Ni at this angle. In addition, ^{58}Ni data were also taken at 48°, well beyond the grazing angle where the spectra were weighted more heavily by highly damped events and fission. No noticeable difference was found in the centroids and variances of the Z and A distribution data as a function of detection angle for energy losses less than ~ 160 MeV.

The channel-plate time-of-flight system and ΔE-ΔE-E gas-ionization detector yielded a net resolution for Ni ions of approximately 0.6 atomic mass units and 0.6 charge units, corresponding to $\Delta A/A \approx 0.010$ and $\Delta Z/Z \approx 0.021$. Figure 1 shows representative Z and A spectra for these measurements over an energy-loss range of 30–200 MeV. Figure 2, which presents a nuclide distribution map over this same energy-loss range, demonstrates the low level of contamination of individual nuclidic yields by neighboring isotopes and isobars.

B. Data reduction

Data reduction procedures generally followed those described in Refs. 12 and 24. However, in performing the laboratory to center-of-mass transformations, important changes were made concerning the assumptions about excitation-energy division and ground-state Q values. Consistent with recent experimental results,[14–17,25] we have assumed that the excitation energy divides according to the equation

$$\frac{E_1^*}{E_2^*}=\frac{A_1T_1^2}{A_2T_2^2}\ . \tag{1}$$

In the absence of experimental excitation-energy division data for the ^{58,64}Ni + ^{238}U reactions, the dependence of the temperature ratio T_1/T_2 on energy loss was taken from the nucleon-exchange trajectory model.[26] The calculations provide a more realistic description of excitation-energy division than does the equal temperature assumption, $E_1^*/E_2^*=A_1/A_2$, used previously. The influence of Eq. (1) in determining the excitation energy division is discussed in Appendix A, where its effect on the data is also compared with previous assumptions. The ground-state Q values, Q_{gg}, were also treated more systematically in this analysis; specifically, for each Z value the Q_{gg} values were treated as a smooth function of mass.

An iterative correction for neutron emission was made in order to obtain primary fragment mass number, A', and neutron number, N'. Based on statistical evaporation calculations,[7,8,14] it was assumed that to first order, charged-particle evaporation is negligible in these reactions and the measured fragment Z values corresponds to

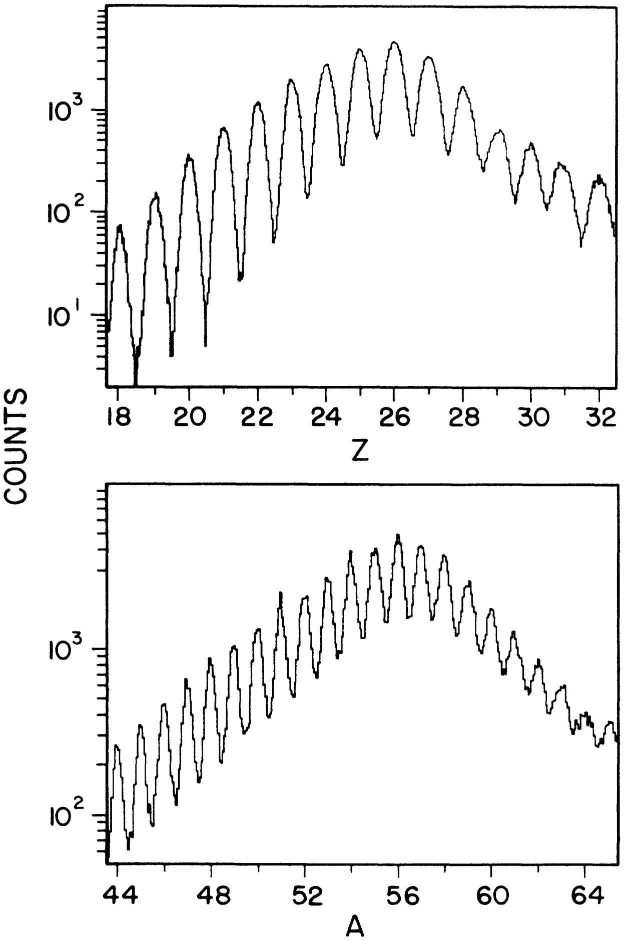

FIG. 1. Top: charge distribution of projectile-like fragments from $E/A = 8.5$-MeV ^{58}Ni bombardment of ^{238}U; energy-loss range is 30–200 MeV. Bottom: mass distribution for same system and E_L range.

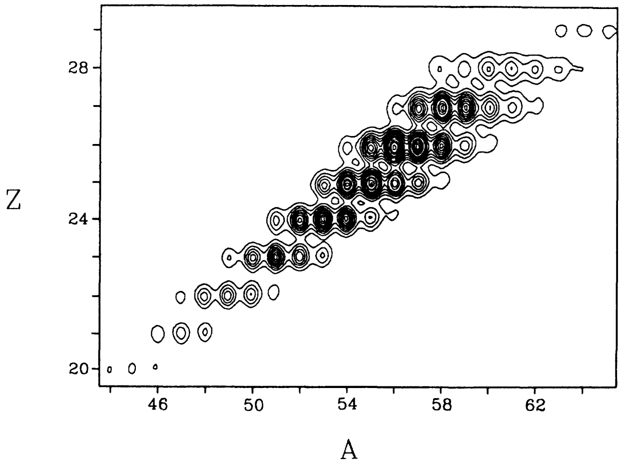

FIG. 2. Cross-section contours of nuclide distribution in $E/A = 8.5$-MeV ^{58}Ni bombardment of ^{238}U; energy-loss range is 30–200 MeV. Cross-section contours are plotted on linear scale.

the primary charge.

The LISA data-reduction program[27] was used to generate one- and two-dimensional spectra in mass number $A(A')$, atomic number Z, and neutron number $N(N')$ for the observed projectile-like fragments as a function of total-kinetic energy (TKE) loss. Examples of these spectra are shown in Figs. 3 and 4.

It has been shown previously[24] that the two-dimensional fitting procedure employed in this analysis is justified by (1) the fact that the average charge is a linear function of A and (2) the isotopic (Z) variance is nearly constant for a major part of the damped cross section. While the major part of the cross section can be well represented with such a procedure, the tails of the experimental two-dimensional $N(N')$ vs Z contours are somewhat skewed toward higher mass values, ecspecially for energy losses greater than 100 MeV. These tails in the large TKE-loss data are commonly attributed to processes other than damped collisions: e.g., fission.

In extracting the parameters of the Gaussian fits to the nuclide distributions, procedures described in Appendix B have been followed. From the least-squares fit with the two-dimensional Gaussian function, described above, fragment centroids ($\langle Z\rangle$, $\langle N\rangle$, and $\langle A\rangle$), variances (σ_Z^2, σ_N^2, and σ_A^2), and neutron-proton correlation coefficients (ρ_{NZ}) were generated. Centroids, variances, and correlation coefficients for these distributions are summarized in Tables I and II for ^{58}Ni and ^{64}Ni projectiles, respectively, and discussed in the following section. Additionally, conditional variances [$\sigma_Z^2(N)$, $\sigma_N^2(Z)$, and $\sigma_Z^2(A)$] were also generated from the data. The two-dimensional Gaussian fitting parameters, as described in Refs. 12 and 24, are listed in Appendix B.

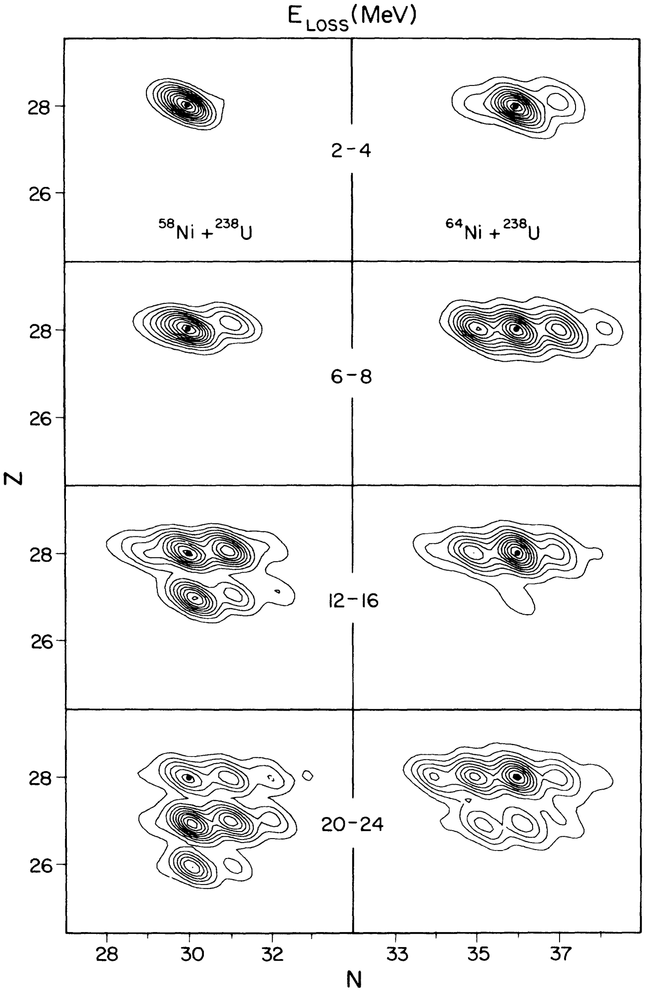

FIG. 3. Cross-section contours for nuclidic yields from the ^{58,64}Ni + ^{238}U reactions as a function of projectile-like fragment N and Z. Energy-loss bins are shown for $E_L = 2-4$, 6–8, 12–16, and 20–24 MeV. E_L has been calculated assuming excitation energy in the reaction divides according to transport model calculations (Ref. 26). Solid circles indicate N and Z of the projectile.

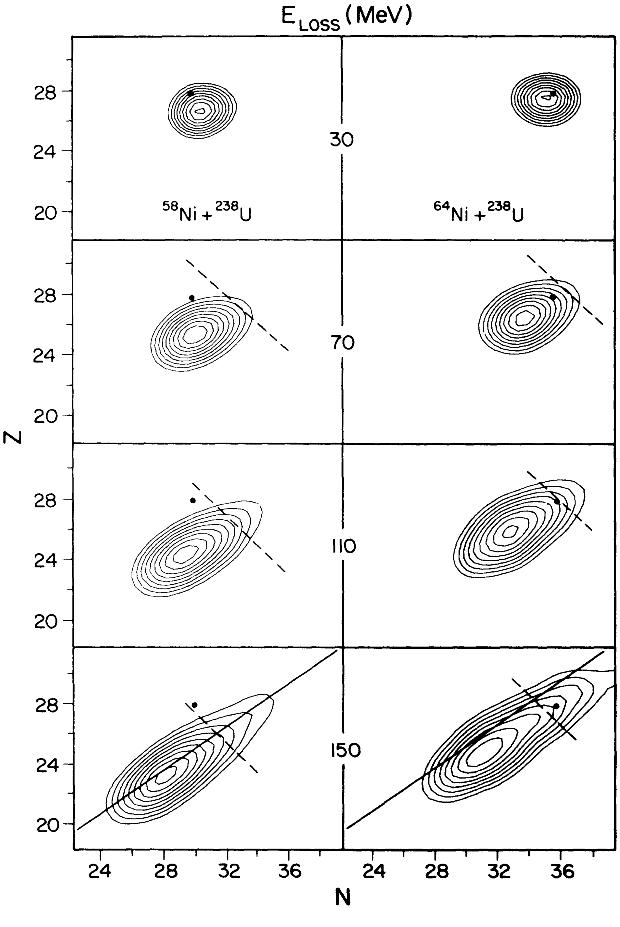

FIG. 4. Smoothed cross-section contours in N and Z for projectile-like fragment yield data for the ^{58,64}Ni + ^{238}U reaction as a function of energy loss. Energy-loss bins for $E_L = 30$, 70, 110, and 150 MeV are shown. The solid circles indicate N and Z of projectile. The solid line indicates the valley of beta stability and the dashed line indicates assumed mass cutoff in damped data, as described in Appendix B.

TABLE I. Proton and neutron centroids, variances, and correlation coefficients for the ^{58}Ni + ^{238}U system.

E (MeV)	$\langle Z \rangle$	$\langle N \rangle$	σ_Z^2	σ_N^2	ρ_{NZ}
4	27.65±0.35	29.94±0.22	0.086±0.154	0.367±0.037	−0.266±0.663
8	27.70±0.05	29.95±0.07	0.107±0.009	0.604±0.010	−0.184±0.023
12	27.62±0.05	30.05±0.07	0.202±0.006	0.868±0.016	−0.153±0.013
16	27.35±0.05	30.24±0.07	0.617±0.020	1.112±0.043	−0.178±0.025
20	27.07±0.05	30.36±0.07	0.727±0.022	0.941±0.026	0.130±0.020
24	26.84±0.05	30.30±0.07	0.848±0.031	1.092±0.034	0.341±0.024
28	26.71±0.05	30.43±0.07	0.892±0.028	1.643±0.040	0.430±0.018
32	26.58±0.05	30.45±0.07	0.743±0.024	1.413±0.038	0.368±0.019
36	26.42±0.05	30.33±0.07	0.714±0.021	1.666±0.38	0.407±0.016
40	26.28±0.05	30.34±0.07	0.852±0.026	1.773±0.041	0.354±0.018
44	26.19±0.06	30.38±0.08	1.022±0.056	2.178±0.97	0.435±0.031
48	26.11±0.05	30.38±0.08	1.049±0.046	2.302±0.089	0.474±0.024
52	25.95±0.05	30.34±0.08	1.120±0.048	2.407±0.094	0.501±0.023
56	25.83±0.05	30.32±0.08	1.278±0.056	2.521±0.102	0.535±0.023
60	25.73±0.05	30.30±0.08	1.390±0.056	2.562±0.092	0.553±0.021
64	25.60±0.05	30.25±0.08	1.503±0.059	2.674±0.095	0.569±0.020
70	25.41±0.05	30.17±0.08	1.638±0.058	2.977±0.098	0.592±0.017
80	25.13±0.05	30.03±0.08	1.936±0.069	3.587±0.128	0.634±0.016
90	24.86±0.05	29.92±0.08	2.106±0.072	4.099±0.141	0.660±0.014
100	24.60±0.05	29.75±0.08	2.396±0.078	4.656±0.155	0.713±0.012
110	24.34±0.06	29.54±0.08	2.728±0.089	5.036±0.168	0.729±0.011
120	24.07±0.06	29.28±0.08	3.120±0.104	5.464±0.185	0.755±0.010
130	23.82±0.06	29.04±0.08	3.458±0.120	5.877±0.207	0.777±0.010
140	23.53±0.06	28.67±0.09	3.951±0.161	6.526±0.269	0.816±0.010
150	23.24±0.06	28.31±0.08	4.139±0.158	6.315±0.243	0.814±0.009
160	22.97±0.07	27.99±0.09	4.842±0.210	7.255±0.320	0.843±0.009
170	22.53±0.07	27.41±0.09	5.224±0.221	7.282±0.312	0.843±0.009
180	22.32±0.07	27.05±0.09	6.108±0.289	8.408±0.402	0.874±0.008

TABLE II. Proton and neutron centroids, variances, and correlation coefficients for the ^{64}Ni + ^{238}U system.

E (MeV)	$\langle Z \rangle$	$\langle N \rangle$	σ_Z^2	σ_N^2	ρ_{NZ}
4	27.83±0.08	35.98±0.11	0.178±0.003	0.727±0.018	−0.297±0.015
8	27.82±0.05	35.82±0.07	0.174±0.003	1.148±0.032	−0.184±0.018
12	27.81±0.05	35.67±0.07	0.217±0.004	1.205±0.029	0.072±0.017
16	27.75±0.05	35.49±0.07	0.276±0.006	1.420±0.042	−0.113±0.018
20	27.66±0.05	35.45±0.07	0.319±0.009	1.229±0.047	−0.094±0.019
24	27.53±0.05	35.45±0.07	0.602±0.008	1.528±0.032	0.050±0.011
28	27.37±0.05	35.29±0.07	0.776±0.022	1.656±0.050	0.059±0.020
32	27.32±0.05	35.17±0.08	0.807±0.041	1.651±0.101	0.071±0.037
36	27.25±0.05	35.08±0.07	0.890±0.030	1.648±0.054	0.067±0.021
40	27.12±0.06	34.87±0.08	1.044±0.055	1.781±0.108	0.151±0.038
44	27.05±0.05	34.80±0.08	1.167±0.048	1.913±0.065	0.283±0.025
48	26.97±0.06	34.68±0.08	1.246±0.065	2.378±0.122	0.355±0.032
52	26.89±0.05	34.56±0.08	1.334±0.050	2.523±0.091	0.354±0.023
56	26.82±0.05	34.40±0.08	1.329±0.051	2.605±0.093	0.404±0.023
60	26.70±0.05	34.33±0.07	1.532±0.049	2.751±0.072	0.443±0.018
64	26.66±0.06	34.28±0.08	1.694±0.100	3.215±0.160	0.472±0.032
70	26.55±0.06	34.03±0.08	1.658±0.081	3.044±0.129	0.428±0.028
80	26.36±0.06	33.77±0.08	1.971±0.094	3.551±0.165	0.557±0.024
90	26.15±0.06	33.52±0.09	2.373±0.123	4.441±0.238	0.607±0.024
100	25.95±0.06	33.20±0.09	2.653±0.138	4.661±0.246	0.655±0.022
110	25.79±0.07	32.99±0.09	3.093±0.177	5.628±0.338	0.687±0.022
120	25.60±0.07	32.63±0.10	3.364±0.183	5.977±0.329	0.720±0.020
130	25.42±0.08	32.35±0.10	3.996±0.253	6.757±0.437	0.770±0.019
140	25.41±0.09	32.16±0.12	4.928±0.347	8.484±0.613	0.794±0.018
150	25.09±0.09	31.77±0.13	5.346±0.409	9.183±0.720	0.833±0.016
160	24.93±0.09	31.42±0.13	5.475±0.424	9.060±0.724	0.835±0.016

III. FRAGMENT NUCLIDE DISTRIBUTIONS

A. General features

In order to gain an overview of the nucleon exchange and N/Z equilibration processes, it is instructive to examine the general evolution of the fragment nuclide distributions at representative energy-loss values. In Figs. 3 and 4, cross-section contours are shown for specific energy-loss bins in the N-Z plane of the measured projectile-like fragment yields. Figure 3 focuses on the quasielastic region ($E_L = 0$–24 MeV), where the number of nucleons exchanged is small. Since the statistical analysis using the two-dimensional Gaussian procedure is subject to analytical uncertainties for data with only a few contributing species and relatively poor energy resolution ($\Delta E/E \approx 1\%$), we present directly-measured N and Z yields for these data. Figure 4 displays the data for larger energy losses, in which the intrinsic nuclide resolution has been randomized to smooth the data.

The development of the nuclide distributions in the early stages of the reaction can be deduced from Fig. 3, where the ^{58}Ni + ^{238}U and ^{64}Ni + ^{238}U systems are compared. In each case the projectile N and Z value is indicated with a solid circle. Energy-loss bins for the measured (secondary) fragments are shown for 2–4, 6–8, 12–16, and 20–24 MeV. For each set of spectra, the center-of-mass energy-loss values have been generated assuming that the excitation energy divides according to predictions of a transport model calculation.[3,26]

For the ^{58}Ni case one observes that initially there is a very strong tendency for the projectile to pick up a neutron from the target to form ^{59}Ni. Neutron pickup is the only open channel for nucleon transfer or exchange at this energy (see Q values in Table III). As soon as sufficient energy becomes available to overcome the negative Q values, there appears to be a strong driving force toward the transfer of a proton from the projectile to the target, or to a lesser extent, exchange of two nucleons with the projectile losing a proton and gaining a neutron. In the 12–16 MeV E_L bin, which is below the threshold for neutron decay (assuming equipartition of the excitation energy[14]), the probability for two-neutron pickup to form ^{60}Ni is markedly less than that for proton loss to form ^{57}Co—despite the very strong Q-value preference for the two-neutron pickup channel. On the other hand, global N/Z equilibration slightly favors the proton-loss process, suggesting the strong influence of chemical potential differences on the earliest stages of the reaction. This is emphasized further at slightly higher E_L (20–24 MeV bin), where the two-proton-loss channel has become comparable to the proton-neutron exchange product ^{58}Co and significantly exceeds the probabilities for one- and two-neutron pickup.

In contrast with the low N/Z projectile ^{58}Ni, the early stages of nucleon exchange with ^{64}Ni evolve much differently. The most Q-value-favored channels involve pickup of either a neutron to form ^{65}Ni or a proton to form ^{65}Cu (see Table III). However, only neutron pickup—which favors global N/Z equilibration—occurs with any significant probability. As the internal excitation energy increases, the failure to populate the Q-value-favored products of higher N and Z is apparent in the data. Most striking is the fact that at $E_L = 6$–8 MeV, ^{63}Ni (Q value $= -4.9$ MeV) competes successfully with the formation of $^{65}_{29}$Cu, $^{65}_{28}$Ni, $^{66}_{28}$Ni, $^{66}_{29}$Cu, and $^{66}_{30}$Zn, all with Q values 4–8 MeV more positive. At this energy loss, proton transfer to the target is energetically forbidden. Thus, the system forms $^{63}_{28}$Ni, which also runs counter to N/Z equilibration forces. This trend persists to higher energy losses, although the yield pattern is modified by the opening of the proton transfer channel to form Co isotopes and the transfer of sufficient excitation energy to permit neutron decay of $^{65}_{28}$Ni, which tends to magnify the yield of $^{64}_{28}$Ni with respect to its neighbors.

TABLE III. Q values for simple nucleon transfer and exchange processes in ^{58}Ni- and ^{64}Ni-induced reactions on ^{238}U.

Projectile nucleon change	^{58}Ni	^{64}Ni
$+1n$	2.9 MeV	-0.1 MeV
$+2n$	9.1	3.8
$+1p$	-4.2	-0.2
$+2p$	-4.7	3.1
$+1p-1n$	-12.5	-5.6
$+1n-1p$	-0.5	-7.5
$-1n$	-7.4	-4.9
$-2n$	-11.7	-5.8
$-1p$	-2.9	-7.3
$-2p$	-2.4	-11.0
$1p+1n$	-0.1	$+0.9$

As a general trend, the dominant feature of the ^{58}Ni distributions is a spreading of the nuclidic yields to lower Z with increasing E_L. Note that in Fig. 3 the directly-measured cross-section contours for individual nuclides (i.e., resolution contours as opposed to nuclide cross-section contours), exhibit an ellipsoidal pattern in the lowest E_L bins that is oriented at 45° to the Z and N axes. This behavior is an artifact of the transformation which converts A to N and does not influence the correlation coefficients, ρ_{NZ}, discussed in Sec. III C.

In Fig. 4 the evolution of the nuclide distributions is shown for a series of E_L values which span the full range of damping for the two systems studied here. Each energy-loss bin corresponds to a ± 5 MeV cut about values of 30, 70, 110, and 150 MeV. On each plot the projectile N and Z are indicated by a solid dot. As will be discussed in the following section, the two systems exhibit quite different behaviors in the drift of their centroids with increasing damping. For ^{58}Ni the neutron pickup plus proton stripping reaction dominates at low energy losses and thereafter proton transfer to the target governs the drift until nearly complete damping is achieved. In contrast, ^{64}Ni-induced reactions exhibit a yield pattern in which nearly equal numbers of protons and neutrons are lost by the projectile rather monotonically over the full E_L range. Part of the neutron loss is, of course, due to statistical evaporation. In both cases the distributions spread uniformly about the centroid at low energy losses and then become elongated along the valley of beta stability as the damping develops. However, while for ^{58}Ni the yield distribution lines up within ~0.5 neutrons of the valley of beta stability (solid line in Fig. 4), for ^{64}Ni the major axis of the yield distribution remains approximately two neutrons to the neutron-rich side of stability, even for fully damped events. The evolution of the centroids, variances, and correlation coefficients are discussed in detail in the following sections.

B. Centroids of the distributions

The centroids of the distributions in Z, N, and A as a function of energy loss are summarized in Fig. 5 and tabulated in Tables I and II. Measured centroids are denoted by squares. As mentioned previously, on the basis of evaporation calculations,[7,8,12] we take the measured charge distributions to be representative of the primary fragment Z values. For neutron and mass numbers, corrections on the observed yields are required to account for the emission of neutrons in the decay of the primary fragments.[12] These primary values, N' and A', are indicated by circles on these and all succeeding plots.

The charge centroids, $\langle Z \rangle$, for the ^{58}Ni + ^{238}U and ^{64}Ni + ^{238}U systems exhibit distinctly different slopes. For ^{58}Ni there is a sharp decrease in proton number at low energy loss followed by a significant, but less pronounced, decrease thereafter. In contrast, the average charge for the ^{64}Ni-induced reaction remains relatively constant at low E_{loss} and decreases slowly thereafter. For ^{58}Ni the average charge transfer is about 3.4 Z units per 100 MeV; for ^{64}Ni this value is about 2.0 Z units per 100 MeV of E_L. Thus, for both systems, the proton drift exhibits quite different behavior although in both cases the net charge flow is from projectile to target.

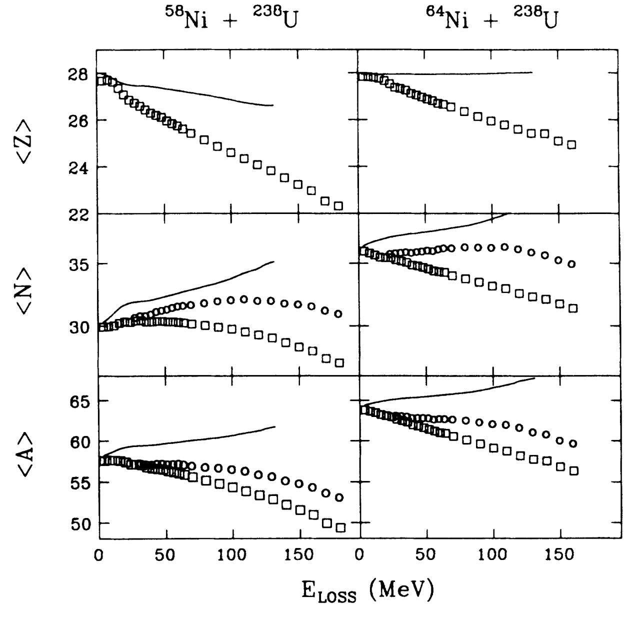

FIG. 5. Centroids of Z, N, and A distributions as a function of energy loss for ^{58,64}Ni + ^{238}U. Measured centroids are designated by squares (□) and derived primary centroids (see text) are denoted by circles (○). Solid lines are predicted primary yields based upon the transport model of Ref. 26.

The centroids of the neutron distributions also contrast in their behavior. For ^{58}Ni the derived primary distributions show an increase in $\langle N \rangle$ as a function of energy loss, leveling off at about $E_L = 100$ MeV with a net gain of about two neutrons. Thus, in the ^{58}Ni + ^{238}U system the net neutron flow goes in the opposite direction of the proton flow. The ^{64}Ni + ^{238}U system experiences a net flow of only about 0.5 neutrons from the target to projectile; hence, this system equilibrates primarily by proton transfer. In terms of the net mass flow, the neutron- and proton-drift behavior—while quite different for the two cases examined here—serve to cancel one another to first order, thereby producing a relatively constant average mass for the damped products as a function of energy loss. The net drifts for the two systems are compared quantitatively in Fig. 6, where the differences between the respective N and Z centroids and the corresponding projectile numbers are plotted. Here we define a parameter $\Delta N(Z)$, which is the difference between the neutron (proton) number of the observed projectile-like fragment and that of the original projectile. Thus, Fig. 6 defines the difference between $\Delta N(Z)$ for ^{64}Ni- and ^{58}Ni-induced reactions.

The rate of N/Z change can be evaluated from Fig. 7,

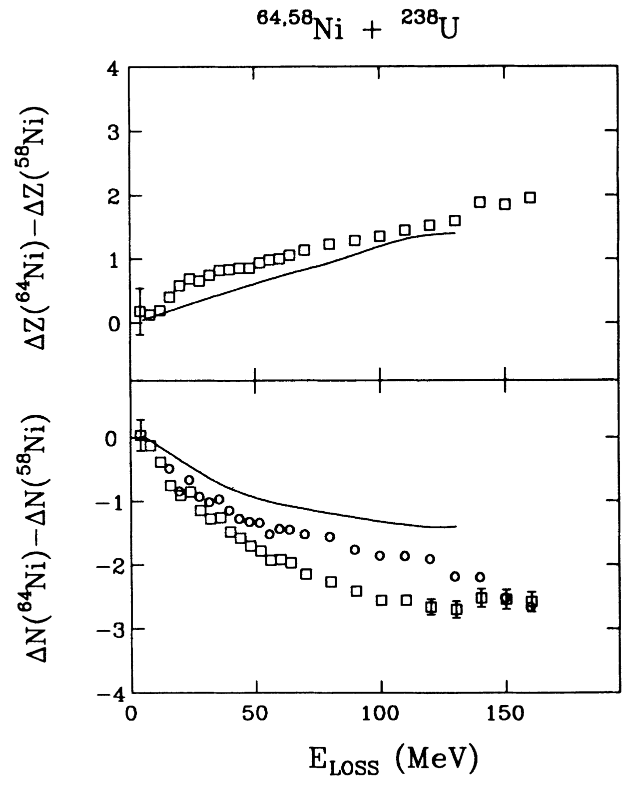

FIG. 6. Difference between Δ values for ^{64}Ni- and ^{58}Ni-induced reactions on ^{238}U as a function of energy loss. The parameter ΔN (lower curve) is defined as the difference between the measured $\langle N \rangle$ of the damped fragment and the neutron number of the projectile. ΔZ (upper curve) is defined similarly for protons. Symbols are the same as those defined in Fig. 5.

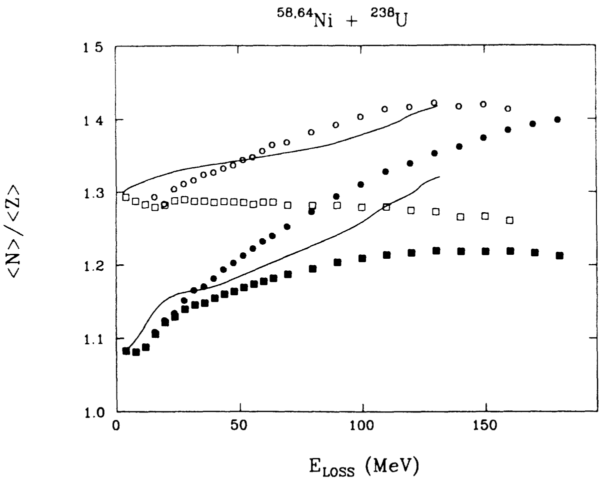

FIG. 7. Ratio of neutron-to-proton centroids as a function of energy loss. Solid symbols are for ^{58}Ni: ■-measured, ●-derived primary; open symbols are for ^{64}Ni: □-measured, ○-derived primary. Other symbols are same as defined in Fig. 5.

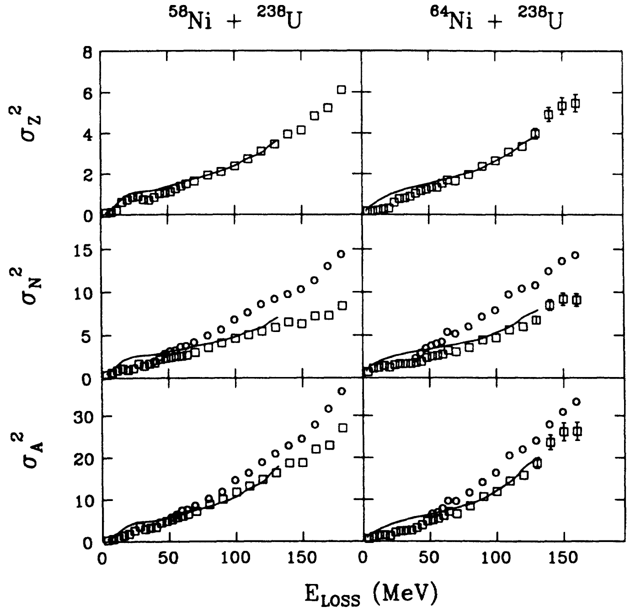

FIG. 8. Comparison of variances for proton (σ_Z^2), neutron (σ_N^2), and mass (σ_A^2) distributions as a function of E_L for ^{58,64}Ni + ^{238}U systems at $E/A = 8.5$ MeV. Symbols are same as defined in Fig. 5.

where the neutron/proton centroid ratios are plotted for both the measured and derived primary distributions as a function of E_L. The comparison between the two projectiles demonstrates the strong correlation between N/Z equilibration and energy loss. It also suggests that the rate of N/Z equilibration is strongly dependent on target-projectile isospin differences, e.g., for ^{58}Ni ($N/Z = 1.07$) this rate is quite large over the full range of damping while for ^{64}Ni ($N/Z = 1.29$) it remains nearly constant over the first 30 MeV of E_L and then drifts slowly upwards. In both cases the ratio of primary $\langle N' \rangle / \langle Z \rangle$ centroids never reaches that of the fully equilibrated composite system, as defined by the minimum in the potential-energy surface. This result suggests in most cases N/Z equilibration does not occur rapidly enough to be completed within the interaction time. In addition, other factors may serve to modify the final nuclide distributions; e.g., the distribution of matter in the neck during scission of the dinuclear complex.[28]

C. Variances and correlation coefficients

Whereas distinct differences exist in the behavior of the Z, A, and N centroids for the ^{58}Ni and ^{64}Ni projectiles, the variances in these distributions exhibit general similarity when plotted versus energy loss. In Fig. 8 values of σ_Z^2, σ_N^2, and σ_A^2 are shown for both the measured secondary and derived primary distributions. These data also show a strong resemblance to the variances observed for ^{56}Fe, ^{48}Ca and ^{40}Ca bombardments of ^{238}U at this E/A value.[12,20] The observed behavior is consistent with the interpretation that if statistical exchange processes form the underlying basis for the nuclidic yields, the variances should differ little for these systems, all of which should have rather similar nucleonic mobilities. On the other hand, the centroids are indicative of the driving forces in the interaction and thus should depend sensitively on projectile-target properties.

The near equivalence of the variances is best illustrated in Fig. 9 where the ratios of the proton and neutron variances for the two systems are plotted versus energy loss. For E_L greater than about 50 MeV, these ratios are nearly constant with a value close to unity. However, for partially-damped events strong variations in these ratios are observed, which can be most simply understood in terms of energetic factors, as discussed in connection with Fig. 3. The negative Q values for proton transfer from ^{64}Ni to ^{238}U, coupled with the hindrance to proton pickup imposed by N/Z constraints results in a narrow charge distribution for ^{64}Ni at low energy losses. This produces a corresponding enhancement of neutron transfer. The net result is increased σ_N^2 and decreased σ_Z^2 values for ^{64}Ni relative to ^{58}Ni. Similar arguments can be used to explain the ratios of the neutron-to-proton variances in each system, as shown in Fig. 10. For both systems the value of σ_N^2/σ_Z^2 exhibits a sharp peak at low energy losses and then decreases to a nearly constant value for the remainder of the energy-damping range. These peaks occur in the E_L region just below the Q-value threshold for proton transfer to the target.

The conditional variances for the two systems are compared in Fig. 11. There is little statistical difference between the ^{58}Ni and ^{64}Ni projectiles as far as the Z variances at constant neutron (or mass) number and N variances at constant proton number are concerned, although the data for the ^{64}Ni-induced reaction appears to be systematically higher. Again, these data are in good general agreement with the earlier ^{56}Fe + ^{238}U results.[12]

Finally, in Fig. 12 the correlation coefficients, ρ_{NZ}, are plotted as a function of energy loss. The correlation coefficient, which can vary from -1 to $+1$, reflects the

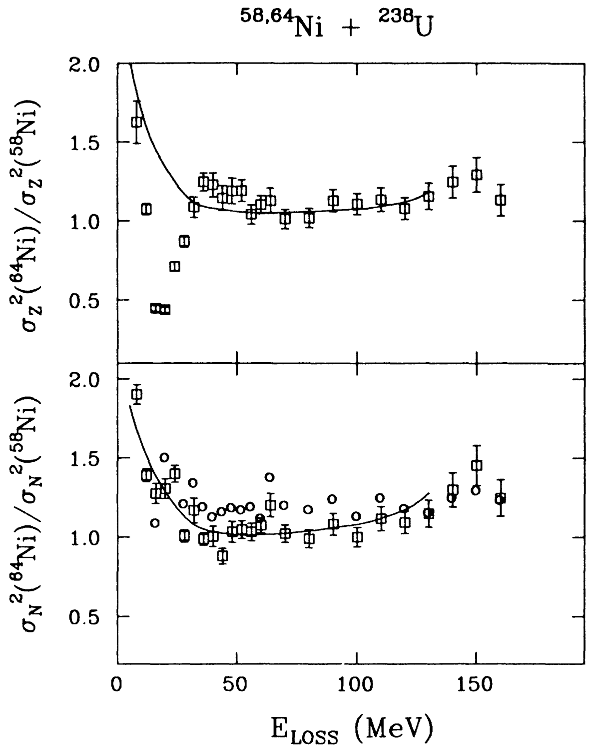

FIG. 9. Top: ratio of charge variance for ^{64}Ni to that for ^{58}Ni as a function of E_L. Bottom: ratio of neutron variance for ^{64}Ni to that for ^{58}Ni as a function of E_L. Symbols are same as defined in Fig. 5.

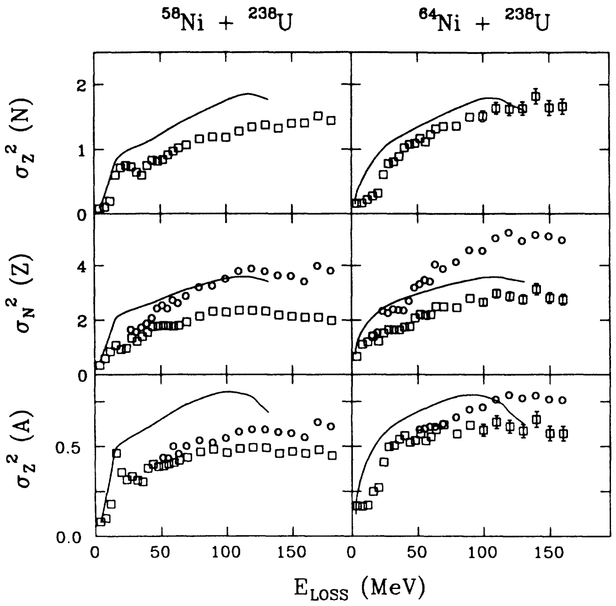

FIG. 11. Conditional variances for ^{58,64}Ni + ^{238}U system as a function of E_L. Top: charge variance at constant neutron number. Middle: neutron variance at constant proton number. Bottom: charge variance at constant mass. Symbols are as in Fig. 5.

relationship between neutron and proton exchanges. Values of $\rho > 0$ correspond to correlated neutron-proton exchange and are indicative of a statistical nucleon-exchange mechanism confined by Q-value constraints to the valley of beta stability. Values of $\rho = 0$ represent uncorrelated exchange. For $\rho < 0$ anticorrelated nucleon exchange is indicated. Such behavior could be evidence for fast charge-exchange mechanisms[9-11] which might be expected in the early phases of the collision, but can also arise from simple manifestitations of the Q values involved. The data shown in Fig. 12 increase monotonically from uncorrelated behavior at low energy losses ($\rho \approx 0$) to near the fully correlated limit ($\rho \approx 1$) for fully damped events, in good agreement with a statistical exchange mechanism for mass and charge transfer.

At very low energy losses, the small number of species which comprise the nuclide distributions complicate the statistical treatment of ρ_{NZ}. For this reason, the slightly negative values of ρ_{NZ} observed in Fig. 12 for energy losses below 20 MeV should be interpreted with caution. We note that the negative values of ρ_{NZ} observed in this work are significantly closer to zero than for the ^{56}Fe + ^{238}U system[12] reported previously. We interpret this difference to be due at least in part to the larger number of bins used in the data-analysis procedures for the

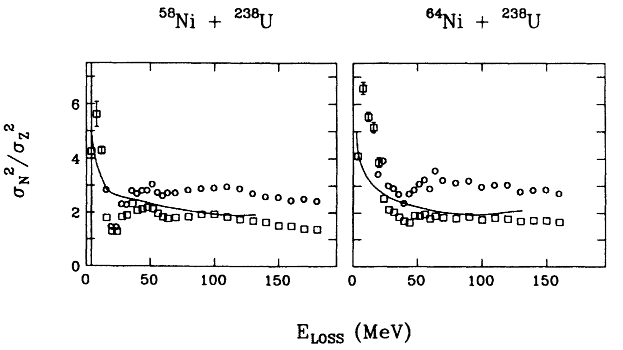

FIG. 10. Ratio of neutron variance to proton variance as a function of E_L for ^{58,64}Ni + ^{238}U systems. Symbols are as defined in Fig. 5.

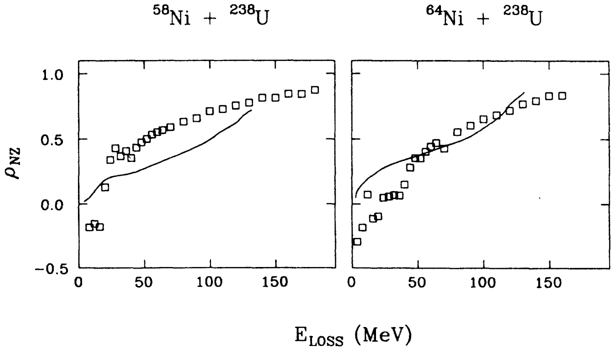

FIG. 12. Correlation coefficient for ^{58,64}Ni + ^{238}U system as a function of E_L. Symbols are as in Fig. 5.

present work, thereby reducing contributions from resolution uncertainties. For larger energy losses, the correlation coefficients become positive and increase rapidly up to about 50 MeV of energy loss. Thereafter, there is an approximately monotonic increase which approaches the fully correlated limit at the maximum energy-loss values. It is observed that for the ^{58}Ni + ^{238}U system, ρ increases more rapidly as a function of energy loss than for the ^{58}Ni + ^{238}U case.

IV. COMPARISON WITH TRANSPORT MODEL CALCULATIONS

Several transport models have been proposed to account for the experimental observables for damped collisions,[3-6] each involving different mechanisms for the dissipation of energy. In the present analysis we have compared the data for the ^{58}Ni + ^{238}U and ^{64}Ni + ^{238}U systems with the dynamic reaction model of Randrup.[3] In this model all transport phenomena are attributed to the exchange of independent nucleons between the reaction partners. The salient transport coefficients are calculated from the instantaneous condition of the dinuclear complex, the constituents of which are always considered to be in intrinsic thermodynamic equilibrium. The reaction variables $\{q_i\}$ include the charge Z and mass A of the fragments. The average values $\{\bar{q}_i,\dot{\bar{q}}_i\}$ of the macroscopic coordinates and velocities follow the equations of motion determined by the Lagrange-Rayleigh equations,

$$\left[\frac{d}{dt}\frac{\partial}{\partial\dot{\bar{q}}_i}-\frac{\partial}{\partial\bar{q}_i}\right]L=-\frac{\partial}{\partial\dot{\bar{q}}_i}F\ , \tag{2}$$

where the subscript i runs over all reaction variables. The quantity $L=T-V$ is the Lagrangian and F is the Rayleigh dissipation function describing the conversion of kinetic energy of relative, tangential, and neck motion into intrinsic heat energy. The driving forces affecting the evolution of the collective variables can be separated into static and dynamic components.

In this model, the fluctuations in N and Z about the average values are predicted by a Fokker-Planck equation,

$$\frac{\partial}{\partial t}P(N,Z,t)=\left[-\frac{\partial}{\partial N}v_N-\frac{\partial}{\partial Z}v_Z+\frac{\partial^2}{\partial N^2}D_{NN}+\frac{\partial^2}{\partial Z^2}D_{ZZ}\right]P(N,Z,t)\ , \tag{3}$$

describing the time dependence of the joint probability distribution $P(N,Z,t)$ for finding N neutrons and Z protons at time t in one of the reaction partners. Drift and diffusion coefficients, v and D, respectively, have been calculated microscopically by Randrup.[3] The above dynamical transport calculation predicts the first and second moments of the proton (Z) and neutron (N) number distributions, as well as the excitation energies of the primary reaction fragments.

The results of the theoretical calculations, explained in more detail elsewhere[26] are shown as solid lines in Figs. 5–12. Without question, the most significant divergence between experiment and model predictions is found for the centroids shown in Fig. 5. The experimental drift in Z is observed to be larger than predicted by the transport model for both projectile-target systems, while for the drifts in N and A the drift is much smaller than predicted.

The differences between the calculated and measured evolution patterns of the N vs Z centroids in the N-Z plane are traced as a function of energy loss for the two Ni projectiles in Fig. 13. For reference we have also plotted in Fig. 13 lines representing (i) the line of maximum beta stability for projectile-like fragments and (ii) the vector indicating the gradient of the potential energy surface at the injection point. The length of each gradient vector is indicative of the strength of the potential gradient. Calculation of the potential energy surfaces were performed according to the relation

$$V=Q_{gg}+V_N+V_l+V_c\ , \tag{4}$$

where the ground-state Q value, Q_{gg}, was calculated from the liquid-drop mass formula with shell corrections and suppression of pairing effects.[29] The nuclear potential V_N was also based on the liquid-drop model with the modified proximity potential of Swiatecki.[30] The centrifugal potential, V_l, and the Coulomb potential, V_c, were those assumed in the transport model of Ref. 26. The gradients shown in Fig. 13 and subsequent figures were calculated for angular momenta just below the grazing value, 240$\hbar$ and 280$\hbar$ for ^{58}Ni and ^{64}Ni, respectively, for a projectile-target distance

$$r=(R_{1/2})_T+(R_{1/2})_P+0.2\ \text{fm}\ .$$

The direction of these gradients depends only slightly on the interaction radius; for example, for the half-density radius $r=R_{1/2}$ or $r=R_{SA}$, the magnitude of the gradient vector changes only by about 10%.

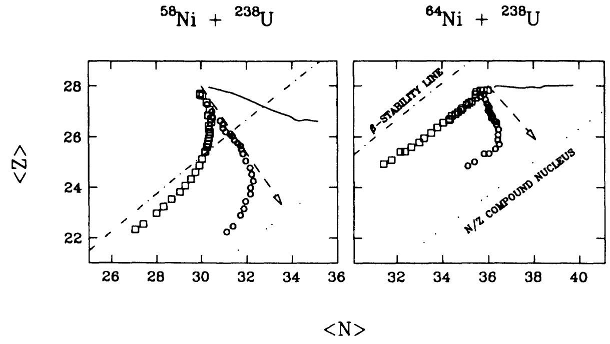

FIG. 13. Evolution of proton and neutron centroids in the N-Z plane for ^{58}Ni and ^{64}Ni reactions with ^{238}U. Symbols are as in Fig. 5. Points reflect successive energy-loss intervals, beginning with low energy losses at Z and N of projectile and evolving toward Z and N of fully damped system (see Fig. 5). The line of maximum beta stability is indicated by the dot-dashed line and the N/Z ratio of the compound system is given by the dotted line. The vector indicates the direction and magnitude of the gradient in the potential energy surface at the injection point.

Figure 13 illustrates in more graphic fashion the strong differences in behavior between the experimental and transport-model (solid line) centroids. Whereas the transport model strongly favors the transfer of neutrons from the target to the projectile to achieve N/Z equilibration, the experimental data indicate a preference for proton transfer from projectile to target. On the other hand, it is observed that the evolution of the experimental primary data in the N vs Z plane correlates rather well with the calculated gradients of the potential energy surfaces at the injection point, both in terms of magnitude and direction. Because the PES is a dominant factor in the transport model for determining the direction of neutron and proton transfers, the deviation of the calculated trajectory from the direction of steepest gradient is somewhat puzzling. A possible source of this difference may be due to different mobilities of transferred neutrons and protons. For example, one such source may be the neutron-skin correction in the model, which serves to enhance the mobility for neutrons exchanged between target and projectile. However, a smaller mobility for exchanged neutrons—which appears to be required to reproduce the $\langle N \rangle$ data of Fig. 5—will also lead to smaller variances for σ_N^2 than those shown in Fig. 8, thus creating a more pronounced disagreement with the variance data. It could be argued, however, if a significant neutron skin exists for ^{238}U, then the neck region that develops during the early stages of contact in the collision will be highly neutron rich. Because the surface neutron density for the projectile is much smaller than that for the target, there will be a strong driving force for protons to flow from the projectile into this neutron-rich region in order to minimize the total isospin. Such a mechanism, which at present is not contained in the model, would provide a means of explaining the general trend of charge drift toward symmetry observed in these and other damped collision systems.

Another possible source of the deviation between the experimental and calculated values may be associated with the temperature equilibration process. As discussed in Ref. 14, excitation-energy transfer proceeds in the direction of nucleon transfer, thus exerting an important influence on the nucleon-exchange process.

Finally, with respect to the centroids it is of interest to note that the ratio of $\langle N' \rangle / \langle Z \rangle$ is predicted rather well by the calculations (Fig. 7), despite the significant absolute deviations for $\langle N' \rangle$ and $\langle Z \rangle$.

Whereas the behavior of the Z, N', and A' centroids indicate the need for important modifications to the transport model, the general agreement between calculated and experimental variances in Figs. 8–10 lends further support to the assumption that statistical nucleon exchange is the basic mechanism governing the damped collision process. At low energy losses the model tends to overpredict the variances, but the observed deviations can be most readily interpreted as due to the influence of Q-value effects in the quasielastic region. At moderate-to-large energy losses the proton variances are described quite well; in contrast the variances for the derived primary neutron and mass distributions exceed the theory somewhat. The more sensitive conditional variances (Fig. 11) are also in general agreement with the experimental values, although significant deviations are observed. The calculated correlation coefficients (Fig. 12) reproduce the data moderately well, especially for ^{64}Ni + ^{238}U above 50 MeV of energy loss. The ^{58}Ni + ^{238}U predictions at E_L values between 20–120 MeV are significantly lower than the data. Thus, while the qualitative features of the variances and correlation coefficients are reproduced by the model calculations, quantitative differences exist which point to the need for some further improvements in the model.

V. SUMMARY

The charge equilibration process in damped collisions has been examined by measuring discrete nuclidic distributions for the ^{58}Ni + ^{238}U and ^{64}Ni + ^{238}U reactions at $E/A = 8.5$ MeV. These data demonstrate that N/Z equilibration is a continuous process that is strongly associated with energy loss over the full range of damping. Equilibration appears to develop more rapidly for the ^{58}Ni-induced reaction, where the N/Z mismatch between target and projectile is greater. However, it is only for the largest energy losses (≥ 180 MeV) that the N'/Z centroid ratio approaches that of the fully equilibrated composite system which corresponds to the minimum in the PES. This suggests that for most of the damped cross section, N/Z equilibration does not occur rapidly enough to be completed within the interaction time.

The importance of isospin driving forces in the very early stages of damping (Fig. 3) is reflected by the strong tendency for proton transfer to ^{238}U, contrary to the Q-value favored path in the opposite direction (Table III). This tendency for proton transfer persists over the full range of energy damping, but is significantly stronger in ^{58}Ni than in ^{64}Ni. This is a systematic feature of damped collisions between asymmetric collision partners, and has now been observed in several systems.[1]

In Figs. 14 and 15 we show the changes in the charge and neutron centroids relative to the projectile for five projectiles incident on ^{238}U at $E/A = 8.5$ MeV, spanning N/Z ratios from 1.00 to 1.40. In Fig. 14 the difference between the measured proton (neutron) centroid and that of the projectile is plotted as a function of energy loss for ^{40,48}Ca, ^{56}Fe, and ^{58,64}Ni. Figure 15 shows the centroid data from Fig. 14 at an energy-loss value of 100 MeV as a function of projectile N/Z. Also shown by crosses are the corresponding values of the gradient of the potential energy surface at the injection point for each system (right-hand scale). One observes that both the experimental charge and neutron drifts behave systematically as a function of projectile N/Z ratio, illustrating the important influence that this degree of freedom exerts on the product yields. Correspondingly, the importance of the PES gradient is reinforced in Fig. 15. One interesting deviation in these systematics is the significantly larger neutron drift for ^{64}Ni relative to ^{56}Fe and ^{48}Ca. Whereas the experimental values of ΔN for ^{56}Fe and ^{48}Ca fall well above the calculated gradient reference points, that for ^{64}Ni falls significantly below. Of the five projectiles compared in these plots, all of the nucleon (N and Z) numbers

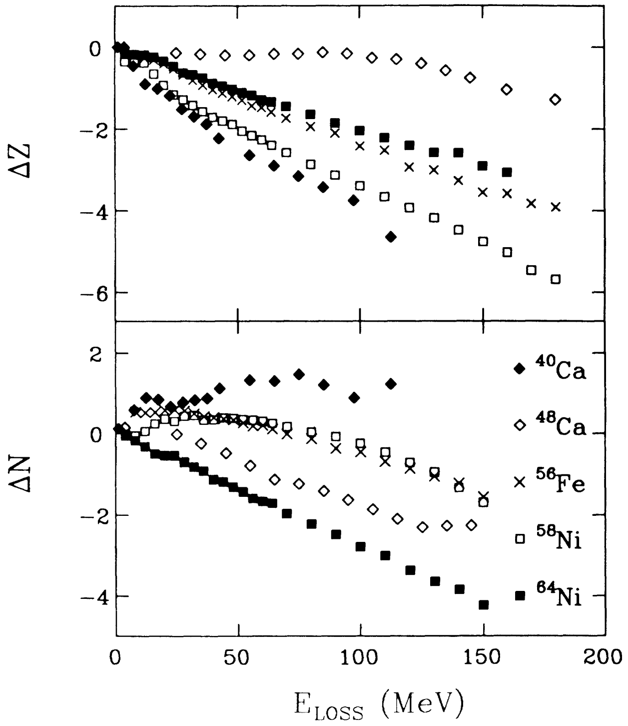

FIG. 14. Upper plot: measured difference between proton centroid and projectile charge as a function of E_L for bombardments of $E/A \cong 8.5$-MeV ^{40}Ca, ^{48}Ca, ^{56}Fe, ^{58}Ni, and ^{64}Ni ions on ^{238}U. Lower plot: difference between secondary neutron centroid and projectile neutron number for same systems. Symbols are indicated on figures.

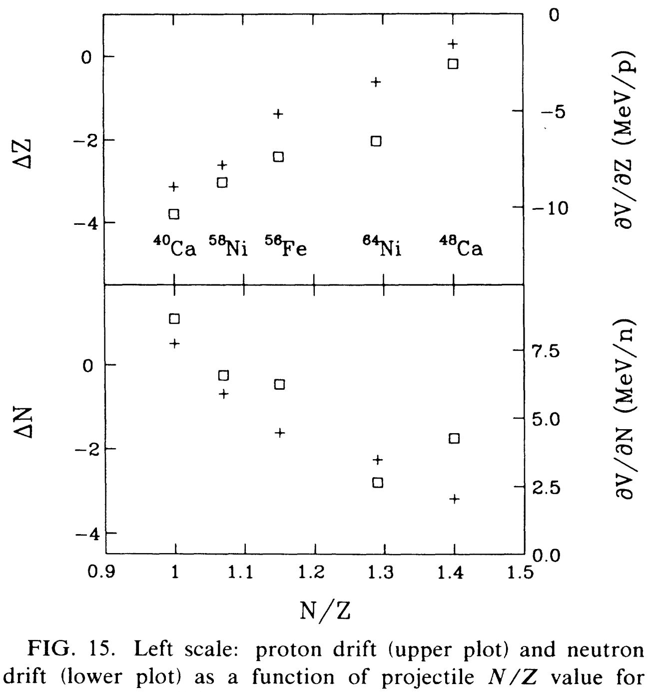

FIG. 15. Left scale: proton drift (upper plot) and neutron drift (lower plot) as a function of projectile N/Z value for $E/A = 8.5$-MeV ^{40,48}Ca, ^{56}Fe, and ^{58,64}Ni ions incident on ^{238}U. All values are taken at an energy loss of $E_L = 100$ MeV. Right scale: values of the gradient in the potential energy surface at the injection point (+) for system, as described in text. In this representation, negative gradients are defined to be directed toward the minimum in the PES.

are very near a closed shell, except for ^{64}Ni, which has $N=36$. The observed behavior may thus be indicative of dynamic effects associated with the deformability of ^{64}Ni.

Attempts to account for the centroid drift toward asymmetry in terms of a transport model[3,22,26] reveal the need for either a more realistic treatment of the isospin degree of freedom, or for additional dynamical features in the theory. Despite this difficulty the overall statistical nature of nucleon exchange in damped collisions is supported by the variance data. Both the ^{58}Ni and ^{64}Ni systems exhibit similar behavior for the variances, and both are predicted relatively well by the transport-model calculations.

ACKNOWLEDGMENTS

This work was supported by the U.S. Department of Energy and the National Science Foundation. The authors wish to thank several individuals whose support in conducting this experiment was invaluable; among these are Bill Elwood, Tom Gee, Gil Hartley, H. Spieler, and Gordon Wozniak at the Lawrence Berkeley Laboratory (LBL); John Dorsett and Dick Yoder at Indiana University, and Walter Kehoe at Maryland. We also acknowledge the excellent nickel beams provided by Harvey Styvesrud and the operating staff at the LBL SuperHILAC.

APPENDIX A: LABORATORY TO CENTER-OF-MASS TRANSFORMATION

As discussed in Sec. II B, laboratory to center-of-mass transformations were performed assuming a binary reaction mechanism and excitation energy division given by Eq. (1). Fragment temperatures were taken from transport model calculations,[26] consistent with recent experimental results.[14-17,25] While this procedure gives a more realistic description of observed experimental results, it complicates comparison with previous nuclide distribution data for asymmetric systems, which assume excitation energy division according to fragment mass ratio.

To check the influence of assumptions concerning excitation-energy division on the centroids and variances of the distributions, data for the ^{64}Ni + ^{238}U reaction are compared in Fig. 16 for two cases: (1) division according to the transport model[26] (solid lines represent observed data and dot-dash lines are data corrected for neutron evaporation), and (2) division according to mass ratio (dashed lines give observed data and dotted lines are corrected for neutron emission). For the measured secondary proton and neutron centroids below $E_{\text{loss}} = 150$ MeV, the deviation between the two assumptions is the order of 0.5 nucleons, just slightly greater than the systematic error limits for these data. Similarly, the experimental variances are not modified strongly. However, for the neutron-corrected primary data, rather significant discrepancies are observed in both the centroids and the variances. The conclusion to be drawn from Fig. 16 is that comparisons among various data sets can be expected to be self-consistent for the measured distributions, but that whenever evaporation corrections are performed to derive primary data, one can only compare those data

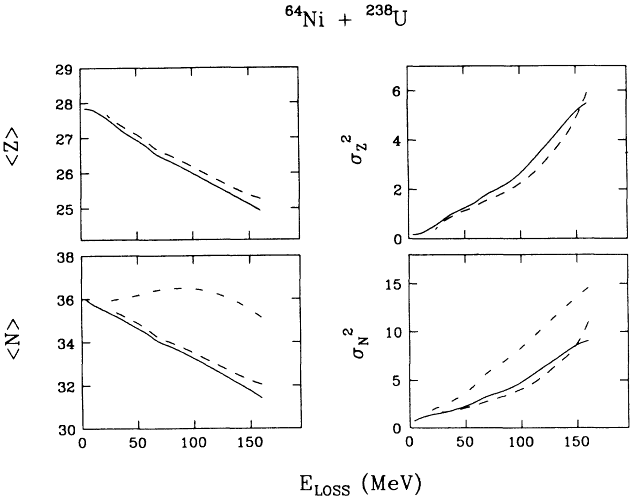

FIG. 16. Influence of assumptions concerning excitation-energy division on the centroids and variances of nuclidic yield distributions for the ^{64}Ni + ^{238}U reaction. Excitation-energy division according to the transport model is given by solid line (measured data) and dot-dashed line (derived primary data). Excitation-energy division according to mass ratio is given by dashed line (measured data) and dotted line (derived primary data).

sets which have treated the excitation-energy-division problem according to the same assumptions.

APPENDIX B: FITTING PROCEDURES

As demonstrated in Fig. 4, the distribution of cross section for fixed energy loss can be generally well represented by a two-dimensional Gaussian function.[12,24] These fitting parameters for the data obtained in this work are tabulated in Tables IV and V. However, at energy losses above 100 MeV the distributions are accompanied by tails skewed toward higher mass values, presumably reflecting the contribution of fully-equilibrated events to the data.

In extracting the parameters of the Gaussian part of the neutron-proton distributions, the following procedures have been followed.

(1) the data were replayed into two-dimensional spectra in $N(N')$ and Z, with gates set on energy loss so that each N and Z value occupied five bins (i.e., 25 bins per nuclide). This increases the numerical grid size relative to that used in Ref. 12 and also reduces the correlation between the experimental resolution and binning effects. The number of points to be fitted was between 100 and 2000. The Gaussian distribution function was folded with the experimental resolution and then fitted to the measured distribution. The widths of the energy-loss gates were chosen to be 4 MeV at low energy losses and 10 MeV at higher values.

(2) In determination of chi-squared fits, only points for which the relative value of the fitting distribution function greater than a fixed limit were taken. Variation of the limit from 0 to 20 % of the maximum for a given energy loss was found to introduce non-negligible changes

TABLE IV. Two-dimensional Gaussian-fit parameters for the ^{58}Ni + ^{238}U system (Refs. 12 and 24).

E (MeV)	a'	b'	k
4	12.747±25.045	2.6702±0.0815	−0.164±0.384
8	9.722±0.815	1.6448±0.0271	−0.094±0.011
12	5.095±0.145	1.1442±0.0206	−0.096±0.008
16	1.734±0.055	0.8677±0.0333	−0.275±0.039
20	1.465±0.048	1.0142±0.0289	0.415±0.056
24	1.612±0.075	0.7577±0.0212	0.695±0.048
28	1.598±0.062	0.5235±0.0123	0.512±0.021
32	1.743±0.067	0.6322±0.0168	0.449±0.022
36	1.855±0.063	0.5430±0.0123	0.394±0.016
40	1.473±0.051	0.5138±0.0117	0.397±0.020
44	1.367±0.092	0.4051±0.0177	0.448±0.032
48	1.411±0.073	0.3784±0.0144	0.462±0.025
52	1.391±0.068	0.3561±0.0137	0.488±0.024
56	1.324±0.069	0.3285±0.0131	0.544±0.026
60	1.284±0.061	0.3151±0.0111	0.585±0.025
64	1.240±0.058	0.2967±0.0103	0.611±0.025
70	1.191±0.050	0.2649±0.0086	0.611±0.021
80	1.113±0.045	0.2163±0.0077	0.621±0.019
90	1.083±0.041	0.1893±0.0066	0.610±0.016
100	1.124±0.038	0.1623±0.0055	0.632±0.013
110	1.061±0.037	0.1466±0.0049	0.661±0.013
120	1.041±0.035	0.1312±0.0045	0.692±0.013
130	1.040±0.039	0.1194±0.0042	0.713±0.013
140	1.109±0.045	0.1044±0.0044	0.736±0.014
150	1.078±0.043	0.1050±0.0041	0.772±0.014
160	1.100±0.049	0.0894±0.0040	0.787±0.013
170	1.048±0.046	0.0866±0.0037	0.821±0.014
180	1.125±0.054	0.0734±0.0035	0.833±0.014

TABLE V. Two-dimensional Gaussian-fit parameters for the ^{64}Ni + ^{238}U system.

E (MeV)	a'	b'	k
4	6.342±0.106	1.3384±0.0336	−0.187±0.010
8	5.970±0.112	0.8659±0.0242	−0.084±0.008
12	4.630±0.088	0.8288±0.0197	0.037±0.009
16	3.685±0.085	0.7020±0.0210	−0.062±0.010
20	3.175±0.086	0.8110±0.0308	−0.064±0.013
24	1.668±0.022	0.6534±0.0139	0.052±0.011
28	1.297±0.037	0.6021±0.0182	0.076±0.025
32	1.252±0.063	0.6028±0.0370	0.096±0.050
36	1.134±0.038	0.6036±0.0198	0.105±0.033
40	1.009±0.053	0.5451±0.0332	0.261±0.065
44	1.025±0.047	0.4753±0.0159	0.451±0.040
48	1.021±0.056	0.3781±0.0195	0.437±0.041
52	0.953±0.039	0.3561±0.0129	0.440±0.029
56	1.019±0.043	0.3387±0.0121	0.463±0.026
60	0.955±0.037	0.3090±0.0078	0.533±0.023
64	0.896±0.061	0.2637±0.0127	0.525±0.040
70	0.858±0.049	0.2827±0.0118	0.512±0.035
80	0.917±0.049	0.2256±0.0104	0.598±0.029
90	0.845±0.047	0.1776±0.0097	0.604±0.027
100	0.874±0.049	0.1621±0.0086	0.655±0.026
110	0.815±0.045	0.1334±0.0082	0.651±0.025
120	0.843±0.051	0.1226±0.0068	0.674±0.024
130	0.872±0.055	0.1041±0.0068	0.713±0.025
140	0.788±0.052	0.0824±0.0060	0.712±0.024
150	0.891±0.063	0.0746±0.0059	0.724±0.023
160	0.892±0.063	0.0746±0.0060	0.741±0.022

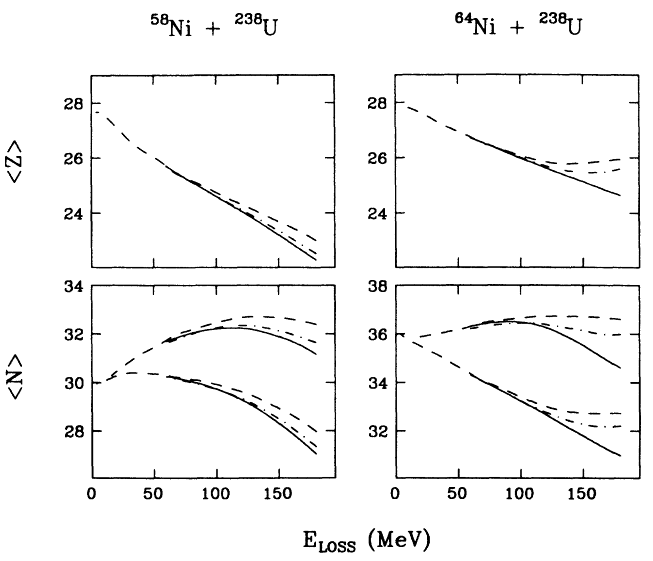

FIG. 17. Effect of Gaussian-fit limits on proton and neutron centroids of projectile-like fragment distributions in the ^{58}Ni and ^{238}U reactions. Dashed (dot-dashed) line shows results of fits which include nuclidic yields greater than 10% (20%) of the maximum yield for a given energy loss. Solid line shows upper mass limit cutoff as defined in Appendix B. For the neutron data the upper set of curves describes the derived primary data; the lower set of curves describes the measured distribution.

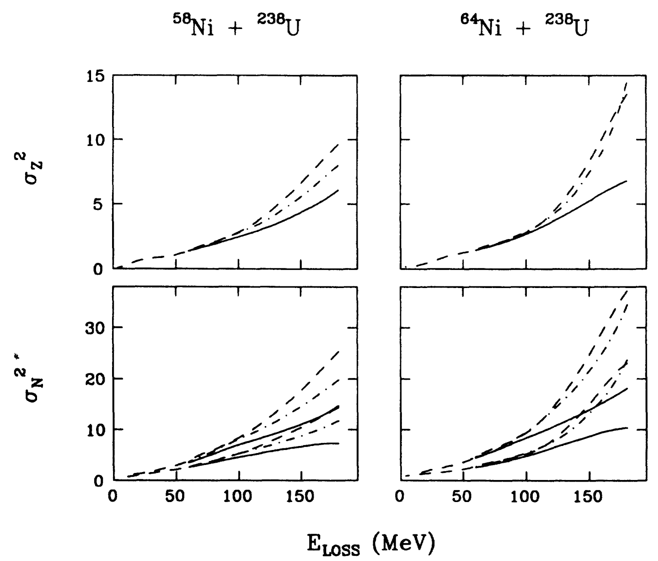

FIG. 18. Neutron- and proton-variance data are compared as described in Fig. 17.

in the fit parameters, especially for energy losses greater than ~150 MeV. Examples of results for 10 and 20% fit limits (dashed and dot-dashed curves, respectively) are compared in Figs. 17 and 18. For the neutron-related data, identical symbols are used for both measured and corrected data, the corrected data always being represented by the upper set of curves. Another approach to minimizing the influence of fissionlike tails on the damped collision distributions is to impose an upper mass cutoff on the data to be analyzed. The solid lines in Figs. 17 and 18 were generated for each energy-loss bin by defining an upper mass limit for analysis that was fixed to be equal to the distance between the mass centroid of the distribution and the mass value at the 10% cross-section level on the low-A side of the distribution. The high-mass cutoff is indicated by the dashed lines in Fig. 4. The centroid and variance results are given by the solid line in Figs. 17 and 18. When extracted in this way, mean values of N, Z, and A agree well with mean values extracted from a 20% fitting limit which includes the high-mass tails of the distributions for energy losses up to 180 MeV for ^{58}Ni and 160 MeV for ^{64}Ni. The influence of the fitting limits is especially strong for σ_N^2 and σ_Z^2 (Fig. 18) where self-consistent fits are obtained only below about 120–140 MeV of energy loss.

Figures 17 and 18 demonstrate that up to an energy loss of 100 MeV, assumptions about the Gaussian fit limits have a relatively minor effect on the results. In addition, it is observed that the ^{64}Ni data are influenced more strongly than that for ^{58}Ni, presumably due to the greater contributions from fission for the more massive, neutron-rich projectile. Clearly, beyond an energy loss of 150 MeV, the fission contribution provides a major perturbation to the damped collision yields, thus making the extracted centroid and variance data dependent on analysis procedures.

---

[*] Permanent address: Institute of Physics, Jagellonian University, Krakow, Poland.

[†] Permanent address: Institute of Atomic Energy, Beijing, People's Republic of China.

[‡] Present address: Kirtland Air Force Base, New Mexico.

[§] Present address: Physics Department, Princeton University, Princeton, NJ.

[**] Present address: Department of Physics, University of Manchester, Manchester, UK.

[1] W. U. Schröder and J. R. Huizenga, *Treatise on Heavy-Ion Science*, edited by D. A. Bromley (Plenum, New York, 1984), Vol. 2, p. 115.

[2] H. Freiesleben and J. V. Kratz, Phys. Rep. **106**, 1 (1984).

[3] J. Randrup, Nucl. Phys. **A307**, 319 (1978); **A327**, 490 (1979); **A383**, 468 (1982).

[4] W. Nörenberg, Z. Phys. A **274**, 241 (1975); Phys. Lett. **53B**, 289 (1974); G. Wolschin and W. Nörenberg, Phys. Rev. Lett. **41**, 691 (1978).

[5] D. H. E. Gross and H. Kalinowski, Phys. Lett. **48B**, 302 (1974); Phys. Rep. **45**, 175 (1978); D. H. E. Gross and K. M. Hartmann, Phys. Rev. C **24**, 2526 (1981).

[6] H. A. Weidenmüller, Prog. Nucl. Part. Phys. **3**, 49 (1980).

[7] D.-K. Lock, R. Vandenbosch, and J. Randrup, Phys. Rev. C **31**, 1268 (1985).

[8] H. C. Britt, B. H. Erkkila, A. Gavron, Y. Patin, R. H. Stokes, M. P. Webb, P. R. Christensen, O. Hansen, S. Pontoppidan,

F. Vidabeck, R. L. Ferguson, F. Plasil, G. R. Young, and J. Randrup, Phys. Rev. C **26**, 1999 (1982).

[9]M. W. Guidry, T. L. Nichols, R. E. Neese, J. O. Rasmussen, L. F. Olivera, and R. Donangelo, Nucl. Phys. **A361**, 275 (1981); M. W. Guidry *et al.*, Phys. Lett. **163B**, 79 (1985).

[10]R. A. Broglia, C. H. Dasso, and A. Winter, Phys. Lett. **53B**, 301 (1974); **61B**, 113 (1971).

[11]H. Hoffman, C. Gregoire, R. Lucas, and C. Ngo, Z. Phys. A **293**, 229 (1979).

[12]H. Breuer, A. C. Mignerey, V. E. Viola, K. L. Wolf, J. R. Birkelund, D. Hilscher, J. R. Huizenga, W. U. Schroder, and W. W. Wilcke, Phys. Rev. C **28**, 1080 (1983).

[13]T. M. Semkow, D. G. Sarantites, K. Honkanen, Z. Li, M. Ross, J. R. Beene, M. L. Halbert, and D. C. Hensley, Phys. Rev. C **37**, 169 (1988).

[14]D. R. Benton, H. Breuer, F. Khazaie, K. Kwiatkowski, V. E. Viola, S. Bradley, A. C. Mignerey, A. P. Weston-Dawkes, and R. J. McDonald, Phys. Lett. B **185**, 326 (1987); and Phys. Rev. C (in press).

[15]T. C. Awes, R. L. Ferguson, R. Novotny, F. E. Obenshain, F. Plasil, S. Pontoppidan, V. Rauch, and G. R. Young, Phys. Rev. Lett. **52**, 251 (1984).

[16]S. Sohlbach, H. Freiesleben, P. Braun-Munzinger, W. F. W. Schneider, D. Schüll, B. Kohlmeyer, M. Marinescu, and F. Puhlhöfer, Phys. Lett. **153B**, 386 (1985).

[17]R. Vandenbosch, A. Lazzarini, D. Leach, D.-K. Lock, A. Ray, and A. Seamster, Phys. Rev. Lett. **52**, 1964 (1984).

[18]B. Gatty, D. Guerreau, M. Lefort, X. Tarrago, J. Galin, B. Cauvin, J. Girard, and H. Nifnecker, Nucl. Phys. **A253**, 511 (1975).

[19]J. V. Kratz, H. Ahrens, W. Bögl, W. Brüchle, G. Franz, M. Schädel, I. Warnecke, G. Wirth, G. Klein, and M. Weis, Phys. Rev. Lett. **39**, 984 (1977).

[20]R. T. de Souza, W. U. Schröder, J. R. Huizenga, R. Planeta, K. Kwiatkowski, V. E. Viola, and H. Breuer, Phys. Rev. C **37**, 1783 (1988).

[21]W. W. Wilcke, J. R. Birkelund, H. J. Wollersheim, A. D. Hover, J. R. Huizenga, W. U. Schröder, and L. E. Tubbs, At. Nucl. Data Tables **25**, 389 (1980).

[22]W. U. Schröder, J. R. Huizenga, and J. Randrup, Phys. Lett. **98B**, 355 (1981).

[23]K. Kwiatkowski, V. E. Viola, W. G. Wilson, S. H. Zhou, and H. Breuer, Nucl. Instrum. Methods **225**, 65 (1984).

[24]H. Breuer, N. R. Yoder, A. C. Mignerey, V. E. Viola, K. Kwiatkowski, and K. L. Wolf, Nucl. Instrum. Methods **204**, 419 (1983).

[25]J. Wile, W. U. Schröder, J. R. Huizenga, and D. Hilscher, Phys. Rev. C **35**, 1608 (1987).

[26]W. U. Schröder, R. T. De Souza, J. R. Huizenga, and L. M. Schnieder, *Proceedings of the International Symposium on Nuclear Fission and Heavy-Ion-Induced Reactions, Rochester, New York, 1986* (Harwood Academic, New York, 1987), p. 255.

[27]B. Kolb, Lawrence Berkeley Laboratory Report No. LBL 16128, 1983; N. R. Yoder (unpublished).

[28]U. Brosa, Phys. Rev. C **32**, 1438 (1985).

[29]W. D. Myers and W. J. Swiatecki, Nucl. Phys. **B1**, 1 (1966); Ark. Fys. **36**, 3413 (1967).

[30]W. J. Swiatecki, Prog. Nucl. Part Phys. **4**, 383 (1980).